Toward Sub-100 ps TOF-PET Systems Employing the FastIC ASIC With Analog SiPMs

A. Mariscal-Castilla, S. Gómez, R. Manera, J. M. Fernández-Tenllado, J. Mauricio, N. Kratochwil, *Graduate Student Member, IEEE*, J. Alozy, M. Piller, S. Portero, A. Sanuy, D. Guberman, J. J. Silva, E. Auffray, *Member, IEEE*, R. Ballabriga, G. Ariño-Estrada, *Member, IEEE*, M. Campbell, and D. Gascón

***Abstract*—Time of Flight positron emission tomography (TOF-PET) scanners demand electronics that are power-efficient, low-noise, cost-effective, and possess a large bandwidth. Recent developments have demonstrated sub-100 ps time resolution with elevated power consumption per channel, rendering this unfeasible to build a scanner. In this work, we evaluate the performance for the TOF-PET of the FastIC front-end using different scintillators and silicon photomultipliers (SiPMs). FastIC is an eight-channel application specific integrated circuit developed in CMOS 65 nm capable of measuring the energy and the arrival time of a detected pulse with 12 mW per channel. Using Hamamatsu SiPMs (S13360-3050PE) coupled to LSO:Ce:0.2%Ca crystals of 2 × 2 × 3 mm^3 and LYSO:Ce:0.2%Ca of 3.13 × 3.13 × 20 mm^3, we measured a coincidence time resolution (CTR) of (95 ± 3) and 156 ± 4) ps full width half maximum (FWHM), respectively. With Fondazione Bruno Kessler NUV-HD LF2 M0 SiPMs coupled to the same crystals, we obtained a CTR of (76 ± 2) and (127 ± 3) ps FWHM. We employed FastIC with a TlCl pure Cherenkov emitter, demonstrating time resolutions comparable to those achieved with the high-power-consuming electronics. These findings shows that the FastIC represents a cost-effective alternative that can significantly enhance the time resolution of the current TOF-PET systems while maintaining low power consumption.**

***Index Terms*—Fast front-end electronics, photo-detector technology, positron emission tomography, scintillator, silicon photomultipliers (SiPMs), Time of Flight positron emission tomography (TOF-PET).**

I. Introduction

NEW DEVELOPMENTS in scintillator-based detectors have significantly improved the image quality of Time of Flight positron emission tomography (TOF-PET) scanners, enabling improved lesion detection [1], [2], [3]. One of the key factors influencing image resolution in these systems is the coincidence time resolution (CTR). CTR is affected by all the components of the detection chain, which compromises the scintillator, the optical sensor, and the readout electronics [4].

Silicon photomultipliers (SiPMs) are currently the most popular sensors for the TOF-PET detectors due to their compactness, low cost, and insensitivity to magnetic fields [5], [6]. These sensors exhibit excellent time resolution and can discern single-photon events [7], [8]. The contribution of SiPMs to the CTR of a PET detector is mainly determined by the photon detection efficiency (PDE) and the single-photon time resolution (SPTR) [9]. For scintillators, the main contributions come from the light transfer efficiency (LTE), the Depth of Interaction (DOI), and the emission probability of the optical photons, which is mainly governed by the intrinsic light yield (ILY) and the scintillation rise and decay time constants [10], [11]. Additionally, DOI and LTE are influenced by the index of refraction and the geometry of the scintillator [12], [13]. Finally, electronics play a key role in the time resolution performance of a TOF-PET system [14]. The contribution of the readout electronics to the detector time resolution is affected by the electronic noise of the front-end electronics and the slew rate (SR) achieved before discrimination for time pick off [15], [16]. Due to the intrinsic capacitance of SiPMs, the electronic noise of the output pulses decreases with the area [15], [17]. Additionally, the internal parasitic resistances and capacitances could also affect the electronic jitter [15].

Standard scintillators based on the LSO:Ce or LYSO:Ce are commonly employed in the TOF-PET detectors due to their excellent timing response [18]. The prompt emission of the

Manuscript received 30 January 2024; revised 23 April 2024; accepted 8 June 2024. Date of publication 14 June 2024; date of current version 5 September 2024. This work was supported in part by the MCIN/AEI/10.13039/501100011033 and by "ERDF A way of making Europe" under Grant PDC2021-121442-100, and in part by the State Agency for Research of the Spanish Ministry of Science and Innovation through the "Unit of Excellence María de Maeztu 2020–2023" Award to the Institute of Cosmos Sciences under Grant CEX2019-000918-M. *(A. Mariscal-Castilla and S. Gómez are co-first authors.) (Corresponding author: A. Mariscal-Castilla.)*

This work did not involve human subjects or animals in its research.

A. Mariscal-Castilla, R. Manera, J. M. Fernández-Tenllado, J. Mauricio, S. Portero, D. Guberman, J. J. Silva, and D. Gascón are with the Department of Física Quàntica i Astrofísica, Institut de Ciències Del Cosmos, Universidad de Barcelona, 08007 Barcelona, Spain (e-mail: antonio.mariscal@fqa.ub.edu; dgascon@fqa.ub.edu).

S. Gómez is with the Departament d'Enginyeria Electrònica, Universitat Politècnica de Catalunya, 08034 Barcelona, Spain (e-mail: sgomez@fqa.ub.edu).

J. Alozy, M. Piller, E. Auffray, R. Ballabriga, and M. Campbell are with the deparment of Microelectronics at Cern, Conseil Européen pour la recherche nucléaire, 1211 Meyrin, Switzerland.

N. Kratochwil is with the Department of Biomedical Engineering, University of California at Davis, Davis, CA 95616 USA.

A. Sanuy is with the Institut de Ciències del Cosmos, Universitat de Barcelona, 08007 Barcelona, Spain.

E. Auffray is with the department of Experimental Physics, Conseil Européen pour la recherche nucléaire, 1211 Meyrin, Switzerland.

G. Ariño-Estrada is with the Department of Biomedical Engineering, University of California at Davis, Davis, CA 95616 USA, and also with the Institut de Física d'Altes Energies-Barcelona Institute of Science and Technology, 08028 Barcelona, Spain.

Color versions of one or more figures in this article are available at https://doi.org/10.1109/TRPMS.2024.3414578.

Digital Object Identifier 10.1109/TRPMS.2024.3414578

TABLE I
INTRINSIC CHARACTERISTICS OF DIFFERENT SCINTILLATORS USED

Composition	Manufacturer	Peak Emission (nm)	Effective decay time (ns)	ILY(ph keV^{-1})
LSO:Ce:0.2%Ca[a]	Agile	420	31.5	39.2
LYSO:Ce[b]	EPIC	420	42	29
LYSO:Ce[c]	Saint-Gobain	420	36	33.2
LYSO:Ce:0.2%Ca[d]	Crystal Photonics Inc.	420	40	45
LYSO:Ce[a]	Crystal Photonics Inc.	420	38.6	41.1

[a] From [18]
[b] EPIC Crystal datasheet: https://www.epic-crystal.com/oxide-scintillators/
[c] Saint-Gobain datasheet: https://www.crystals.saint-gobain.com/
[d] Crystal Photonics Inc., Florida, United States.

pure Cherenkov radiators like TlCl, TlBr, or PbF_2 makes them particularly interesting for fast-timing applications [19], [20], [21], [22]. Recently, the BGO crystals have regained attention due to their ability to generate both the Cherenkov and scintillation photons [23], [24]. Other approaches involve the use of heterostructures, which combine the standard scintillators like LYSO or BGO with prompt emission scintillators [25], [26]. In the case of SiPMs, technology developed by Fondazione Bruno Kessler (FBK) has demonstrated a PDE close to 70% at 420 nm, a SPTR below 50 ps for an intrinsic SiPM of 3× 3 mm^2 and a crosstalk probability of around 10 % at 20 V of overvoltage [27], [28].

In the literature, several application specific integrated circuits (ASICs) have been proposed for the readout of photodetectors that can be used in PET applications, such as the NINO ASIC [29], the Weeroc family (PETIROC2A and more recently RADIOROC) [30], [31], the TOFPET2 [32], [33] ASIC developed by PETsys electronics [34], and the FlexToT family [14], [35], [36], [37], [38]. The best timing performance reported so far was achieved using the so-called high frequency (HF) readout [16], [18], [39]. However, this solution implies the use of discrete components and requires a huge power consumption ($\sim$ 720 mW/channel), which makes it almost impossible to be scaled to a large scanner involving tens of thousands detectors. Recent studies have demonstrated the possibility of achieving a similar performance while using the lower-power amplifiers [40], [41]. But in this case the signal was digitized with an oscilloscope, meaning that the question on how to implement the proposed approach at the system level still remains open.

Several companies and institutions, such as General Electric (GE), United Imaging, Philips, or UC Davis [3], [42], [43], [44] have developed the TOF-PET scanners with a CTR in the range of 250–400 ps. The Siemens biograph vision digital PET/CT scanner provides the lowest CTR achieved at the system level, with a value of $\approx$ 178 ps [45]. Electronics have not been disclosed for those devices.

This work evaluates the application of a multichannel front-end ASIC, known as FastIC [46], [47]. FastIC is a low-power ASIC designed for fast-timing applications. The study focuses on the evaluation of FastIC in conjunction with different scintillators and SiPMs for the TOF-PET scanners. Furthermore, an assessment of the FastIC readout using the pure Cherenkov emitters is provided. All the measurements were conducted using the detectors consisting of one single channel.

In Section II, the main characteristics of the FastIC ASIC and of the SiPMs and scintillators employed are described. Section III details the experimental setups employed. In Section IV, time and energy resolution measurements obtained with scintillators and a Cherenkov radiator are presented. Sections V and VI discuss the results and future improvements.

II. MATERIALS

In this section, the characteristics of the scintillators and SiPMs employed are described. Additionally, the main aspects of FastIC ASIC when configured for the single-SiPM read-out mode are explained.

A. Scintillators

A variety of scintillators were used to evaluate the performance of the FastIC ASIC. Table I summarizes their characteristics, including their light yield, manufacturer, peak emission, and decay time. The scintillators were coupled to SiPMs using either the Cargille Meltmount glue or Saint-Gobain BC-630 optical grease with refractive indices of n_D =1.582 and n_D =1.465 at 588 nm, respectively. All the crystals were wrapped with at least three layers of Teflon. We also evaluated the TlCl crystal, a semiconductor material, manufactured at Radiation Monitoring Devices, Inc. (RMD, Watertown, and MA) with dimensions of 3×3×5 mm^3. TlCl produces prompt photon emission through the Cherenkov emission, with approximately 19 generated photons for 511 keV gamma depositions [20], [21].

B. Silicon Photomultipliers

Several SiPMs were utilized, all with comparable sensitive areas and pixel sizes. The technical specifications and characteristics of the different SiPMs employed are presented in Table II.

HPK S13360-3050CS/PE/VE sensors share similar technical attributes, differing primarily in their respective window materials. The S13360-3050CS SiPM, featuring a silicone resin window (n_D = 1.41), exhibits superior sensitivity to near UV spectrum compared to the S13360-3050PE/VE, which has an epoxy resin window (n_D = 1.55). The S14160-3050HS SiPM sensor also incorporates a silicone window, exhibiting similar PDE behavior as the S13360-3050CS. The S14160-3050HS displays marginally lower PDE at 410 nm, but better SPTR compared to the S13360-3050CS/PE/VE [18].

TABLE II
SPECIFICATIONS OF THE SIPMS EMPLOYED

SiPM	Size (mm^2)	SPAD size (μm^2)	Breakdown(V)	Bias (V)[a]	PDE(%)(λ nm)	Intrinsic SPTR (ps)
HPK S13360-3050CS/PE/VE[a]	3x3	50x50	51.8	62	62 (410)	135 $\pm$ 8
HPK S14160-3050HS[a]	3x3	50x50	38.0	48	60 (410)	117 $\pm$ 6
FBK NUV-HD LF2 NM	3.12x3.2	40x40	32.9	38	65 [a] (410)	65 $\pm$ 2 [b]
FBK NUV-HD LF2 M0	3.12x3.2	40x40	32.8	38	65[a] (410)	50 $\pm$ 2 [b]
FBK NUV-HD-MT LF M0	3x3	40x40	32.5	42.5	68[c] (420)	-

[a] From [18]
[b] From [28]
[c] From [27]

Furthermore, both the S13360-3050VE and S14160-3050HS sensors integrate through the silicon via the TSV technology, eliminating the need for wiring on the photosensitive area side.

Additionally, we evaluated new SiPMs developed by FBK, the FBK NUV-HD low field two nonmask (LF2 NM), FBK low field two mask 0 (LF2 M0), and FBK NUV-HD-metaltrenches low field mask 0 (MT LF M0) SiPMs. FBK NUV-HD LF2 NM and FBK NUV-HD LF2 M0 SiPMs are modified versions of the standard FBK NUV-HD [8], where the electric field has been engineered to be confined within the single photon avalanche diode (SPAD) [28]. This new engineered electric field improves the time resolution of the SiPMs [28]. The FBK NUV-HD LF2 NM and FBK NUV-HD LF2 M0 SiPMs differ primarily in that the latter employs a metal mask applied to the SPAD. This metal mask increases the fast component in the SPAD signal due to the increased quenching capacitance and helps to transport the electrical signal more efficiently to the SiPM anode, resulting in improved single photon time resolution [28]. FBK NUV-HD-MT LF M0 SiPM incorporates metal-filled deep trenches that isolate each SPAD, effectively confining the emitted photons during avalanche within the SPAD. These emitted photons have a high probability of being reflected by the metal trenches, thus not affecting neighboring SPADs. This significantly reduces crosstalk (approximately 10% at 20 V of overvoltage) compared to the FBK NUV-HD, allowing for slightly improved photon detection efficiencies and better time resolution across a wider bias voltage range, particularly advantageous for the large system applications [27].

C. FastIC

FastIC is an eight-channel ASIC developed in CMOS 65 nm technology that can be used for the readout of positive and negative polarity sensors with intrinsic gain, like photomultiplier tubes (PMTs), SiPMs, or michochannel plates (MCPs). It has different configurations that are detailed in [46]. The configuration used in this study is shown in Fig. 1. In this configuration, each input signal outputs a signal with two binary pulses (see Fig. 2). The first binary pulses encoded the time of arrival (ToA) information in its rising edge and the width of the second pulse encode the amplitude information. To accomplish this, three copies of the input signal are produced in the input stage: one is used to extract the time information by using a time discriminator, another one is used for extracting the amplitude information, and the final copy is used to produce a trigger, where the same type of discriminator used in the time branch is used. Additionally, the FastIC has the capability to accept external trigger signals to validate the energy measurement. In the following, the architecture, signal generation, and FastIC module are explained in detail.

1) FastIC Architecture: FastIC architecture is based on a three-branch signal processing which provides a precise timestamp, a linear energy measurement and triggering (see Fig. 1). The front-end stage consists of a low input impedance (approximately 20 Ω up to a few hundreds of MHz) high performance current mirror with two control feedbacks to ensure proper DC operation, maintain a linear behavior over the entire dynamic range and keep low the input impedance over the signal bandwidth. Moreover, it is compatible with a detector capacitance ranging from few pF to nF. The input stage has sufficient gain-bandwidth (GBW) to preserve pulse shapes as narrow as 5 ns FWHM unaltered, and low noise to guarantee the single-photon detection with low electronic jitter contribution. Finally, the input stage has a power consumption of approximately 3 mW. The input stage produces three copies of the input signal read out from the SiPM, with different amplification factors.

The time branch is connected to a leading-edge current comparator allowing to measure the ToA down to the single SPAD signal level. This branch determines the contribution of the ASIC to the time resolution. A nonlinear time over threshold (ToT) measurement can also be provided. This nonlinear ToT provides a nonlinear relation with respect to the number of detected photons, allowing to distinguish between the first few SPADs signals. A binary pulse is generated when the input signal crosses a fixed threshold, both on the rising and falling edges. This threshold can be adjusted by changing an internal register using the slow control mechanism via the serial I2C bus available in the ASIC. The ToA is encoded in the rising edge and the ToT in the width of the generated binary pulse. It processes all the pulses that crosses the discriminator threshold. Its maximum rate is mainly limited by the shape of the input signal. Additionally, the leading edge comparator provides an indirect measurement of the collected charge encoded in the pulse width of the time signal. However, it is important to remark that this charge measurement based on the signal width is nonlinear with respect to the number of detected photons, which complicates its use as an energy estimation, especially for the large input signals.

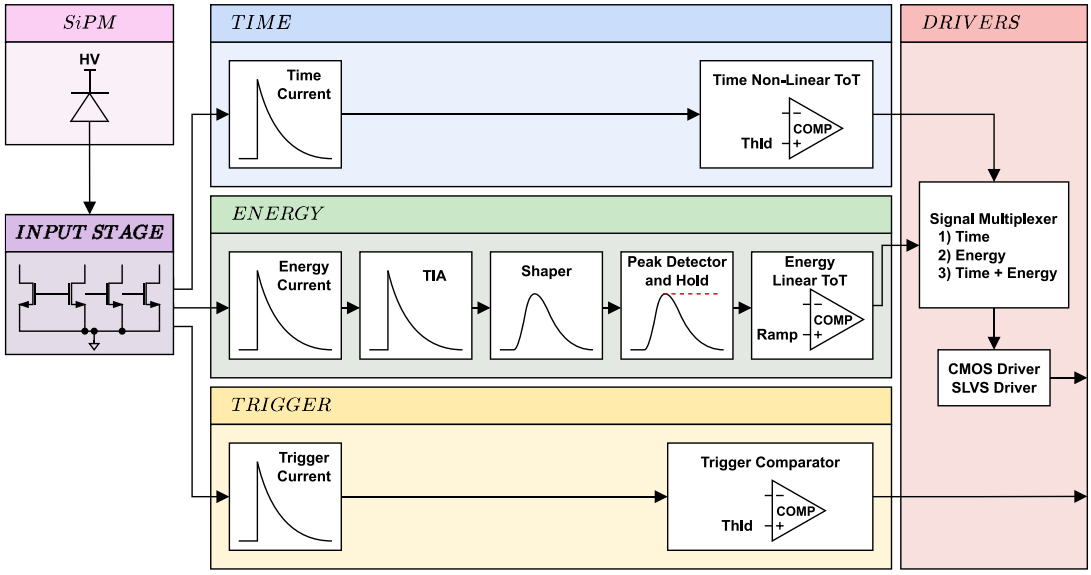

Fig. 1. Block diagram illustrates FastIC's single readout channel for SiPMs suitable for TOF-PET applications.

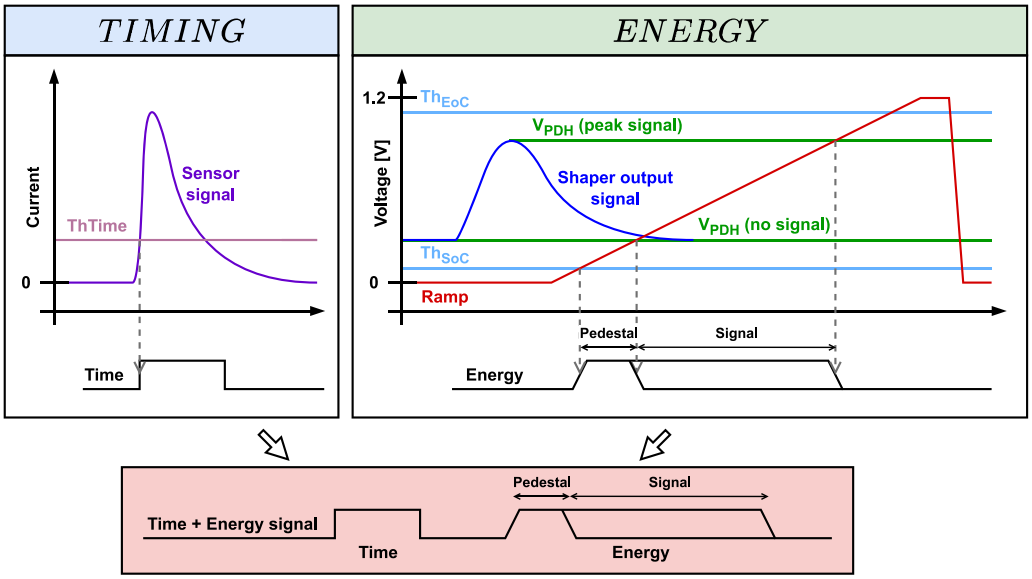

Fig. 2. Schematic representation of the generation of the FastIC time plus energy output signal and the energy acquisition mechanism employed to provide a linear ToT response.

The energy processing branch generates a binary pulse where the pulse width encodes the peak amplitude information of the detected signal, which is directly proportional to the collected charge. The peak amplitude of an SiPM provides a linear measurement of the number of detected photons as long as the SiPM response remains linear. The energy acquisition architecture is as follows. An attenuated (and configurable) copy of the input current is converted into voltage by using a transimpedance amplifier (TIA) with adjustable gain. The dynamic range is primarily constrained by the voltage headroom of this stage, which is determined by the low voltage rail of 1.2 V used in the CMOS 65 nm technology. The TIA is designed with a GBW large enough to cope with fast signals down to 5 ns at FWHM, suitable for fast sensors, such as PMTs or MCPs [46].

The signal pulse shape is conditioned through the passive pole-zero cancelation and a first-order active integrator. The shaper circuit is designed to extend the duration of the rising edge of the input signal, effectively increasing its peaking time. This adjustment reduces the signal requirements (bandwidth and SR) of the subsequent stages. Additionally, it shortens the falling edge to reduce the recovery time or tail of the input signal. This helps mitigate pile-up effects resulting from the correlated and noncorrelated SiPM noisy pulses, such as dark counts, after-pulses, and delayed crosstalk.

After the signal conditioning, the peak detector and hold (PDH) block captures the peak amplitude, which corresponds to the maximum signal value. Simultaneously, a linear ramp (created by a constant current charging a capacitor) is generated and serves as a threshold for a rail-to-rail voltage

discriminator. The linear ramp is compared with the detected peak to encode the energy response in the pulse width of a binary signal. Therefore, the time duration of the binary pulse generated by the comparator is linearly proportional to the detected peak amplitude (i.e., the amount of fired SPADs of the input signal) since both the ramp and the peak amplitude are linear. The pulse generation of the energy measurement is controlled by a synchronous finite state machine (FSM), and as a result the system requires a clock signal to manage the data acquisition process. The same scheme for linearly extracting the amplitude information was used in the HRFlexToT ASIC, but the FastIC uses a synchronous FSM [14]. The maximum hit rate per channel of the linear energy measurement mode is limited to 2 MHz, determined by the duration of the ramp.

FastIC allows for three possible way to validate events in the energy acquisition process: one way is by using the time signal, another one by using an external trigger signal, and the final one is by using the internal trigger signals. The internal trigger signals are generated using the same type of comparator that is used in the time branch. Each channel has a low-level trigger option with a configurable threshold, thereby reducing the acquisition of nonsignificant data, such as dark counts, residual radiation, or low-energy signals. Additionally, a high-level (or cluster) trigger is generated by summing the input signals from all the channels before the comparator. This trigger can be used in the crystal configurations where the signal is distributed across multiple channels [48]. Furthermore, the internal trigger signal is accessible as an OR combination of the trigger signals from each channel.

Time and energy information are encoded as two consecutive pulses as shown in Fig. 2. The output driver can be configured as either the CMOS single-ended or differential scalable low-Voltage signaling (SLVS) modes. Additionally, a speed analog driver capable of driving capacitive loads can be used to monitor the TIA, shaper, and peak detector outputs, which is useful for debugging or waveform sampling. A differential SLVS output is available providing a logic OR between the time signals of all the channels. This feature is valuable in cases where the significant signal is present only in the fastest channel, such as pixelated crystals, for example. Internal registers for controlling the ASIC's various configurations can be managed through a serial I2C bus. Finally, the total power consumption in single readout mode is approximately 12 mW per channel with the default configuration.

2) FastIC Signal Generation: Fig. 2 summarizes the generation of the time and energy signals. The time signal is generated when the input signal's rising edge crosses the discriminator threshold *ThTime*, providing a ToA measurement. Its falling edge is produced when the input signal crosses back the discriminator threshold. Therefore, the width of the time signal contains the nonlineal ToT information about the input signal. For SiPMs, this nonlinear ToT measurement is on the order of hundreds of nanoseconds, so it is arbitrarily shortened to avoid overlap with the energy signal.

The energy signal requires a trigger (i.e., validation) signal to start the acquisition process. As previously stated, this is intended to avoid processing undesired events and as a result, reduce unnecessary data processing. When an event is detected by any of the triggers, the peak detector holds the maximum amplitude of the shaper output (V_{PDH}). After sampling the peak, a linear ramp begins with a DC level below the quiescent voltage of the PDH output. The rising edge of the energy pulse occurs when the ramp crosses the start of conversion threshold, labeled as Th_{SoC}. The falling edge of the energy pulse occurs when the ramp voltage crosses the value captured by the PDH. The end of conversion is detected when the ramp crosses the final threshold, labeled as Th_{EoC}. In this stage, the synchronous FSM prepares the system for a new acquisition by discharging the peak detector (setting the peak detector to operate in tracking mode) and resetting the ramp (the ramp will start again for a new event).

Two scenarios are foreseen for the generation of the energy pulse. In the absence of signal, for instance, when another channel has triggered the acquisition or when using an external trigger, the falling edge is generated when the ramp crosses the quiescent level of the PDH. This pulse, known as the pedestal or minimum energy pulse, captures the baseline variations of the signal at the PDH stage. This pedestal must be acquired before operation (the calibration phase) and must be subtracted from the energy pulse during the data analysis for a precise energy measurement. In the other scenario, the energy measurement is achieved when the ramp crosses the peak voltage captured by the PDH (V_{PDH}).

3) FastIC Module: A custom module was designed for testing the FastIC ASIC. It consists of a stack of two printed circuit boards (PCBs), as shown in Fig. 3(a). The front-end board contains two FastIC ASICs, in order to handle up to 16 channels. Additionally, this PCB also contains power regulators and multiple connectors. The low-voltage terminal powers the ASICs, while the high-voltage terminal biases the SiPMs. This PCB is also equipped with multiple connectors that enable a direct connection to the input channels of the FastIC ASICs, allowing for the direct attachment of the SiPMs to the PCB.

Fig. 3(b) offers a detailed view of the control board located on the bottom. The bottom PCB houses an FPGA mainly used for the slow control of the ASIC through a serial I2C bus and thereby it enables to configure the registers of the ASIC. It also contains an USB driver to communicate with a computer for the data analysis. Data acquisition can be performed by either reading the output signals from the front-end board with an oscilloscope/digitizer or by employing an FPGA-based time-to-digital converter (TDC). This control board includes an FPGA-based TDC IP core with 17 channels, one for the trigger and 16 for the individual outputs. This block converts binary input signals into digital form by using the built-in fast carry-sum logic of the FPGA, known to be the highest-speed FPGA delay element. For this application, a Speed Grade 7 Intel MAX 10 FPGA was utilized, resulting in a differential nonlinearity (DNL) or jitter of approximately 66 ps FWHM. In this work, the TDC is only employed to measure the energy resolution achieved with the FastIC, but its use can be extended for the CTR measurements. We avoid using this TDC in CTR measurements to prevent a significant degradation in time resolution, which would mask the benefits of FastIC.

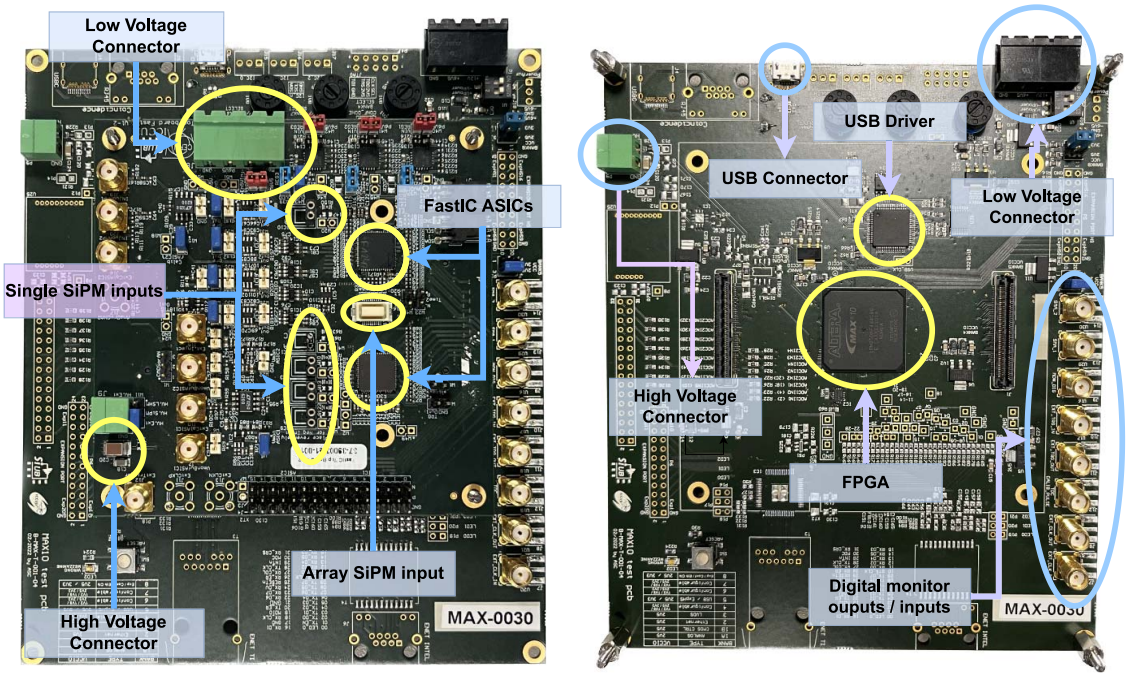

(a) (b)

Fig. 3. FastIC module designed to test the FastIC ASIC. (a) Picture of the complete module showing the front-end board with two FastIC ASICs. (b) Picture of the control board containing an Intel MAX 10 FPGA.

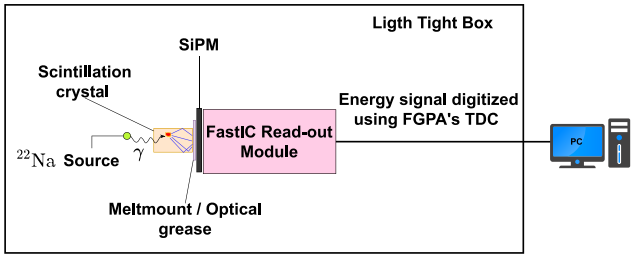

Fig. 4. Schematic representation of the experimental setup employed to evaluate the energy resolution.

III. Methods

This section provides a comprehensive outline of the experimental configurations employed for assessing the performance of FastIC. A thorough description is provided for the energy spectroscopy and the CTR measurements for the scintillators and Cherenkov radiators.

A. Energy Resolution

The energy resolution was studied using a detector composed of an HPK S13360-3050PE SiPM coupled to an LYSO:Ce:0.2%Ca crystal of 3.13 × 3.13 × 20 mm^3. The crystal and the SiPM were coupled using the Meltmount. The sensor signal was read by a FastIC ASIC and digitized by a TDC implemented in an FPGA (see Fig. 4).

The linearity of the energy branch was previously evaluated using an arbitrary waveform generator to inject an electrical pulse that emulated the SiPM response, achieving a linearity error of less than 3% across its entire dynamic range, which extends up to approximately 20 mA [47]. In SiPMs, the output pulse is proportional to the number of fired SPADs when this number is significantly different from the total number of SPADs in the device. When the number of fired SPADs crosses a certain number, the detector saturates. This number depends on the availability of SPADs to detect succeeding photons while a portion of the SPAD population is recovering from the detection of the preceding photons [49]. In this case, the saturation effect of the S13360-3050PE SiPM was corrected employing the method detailed in [14]. This method calibrates the energy response measured in ns into keV by performing a linear regression of several calibration points. In this case, the characteristics peaks of the ^{22}Na source were employed, i.e., the 511 and 1.27 MeV photoelectric peaks and their corresponding Compton edge and backscatter peaks.

B. Coincidence Time Resolution Using Scintillators

The CTR was evaluated using the standard setup for the TOF-PET detector assessment [14], [18] (see Fig. 5). In our setup, inorganic scintillators were coupled to the SiPMs using the Meltmount. The same setup was also employed to compare the performance of the FastIC with respect to the HRFlexToT.

The setup operates as follows: a ^{22}Na source positioned in the center emits a positron that is annihilated with an electron, resulting in the emission of two gamma photons with the anti-parallel linear momenta. These photons are converted by inorganic scintillators in optical photons that are collected by the analog SiPM generating an electronic signal. This signal is then processed by the FastIC. Time and energy outputs from each FastIC board are connected to an Agilent MSO9404 (4 GHz, 10GSa/s, and 8 bits ADC) oscilloscope where the time delay between both the time signals and the width of both the energy signals are measured (Fig. 5). The time signal

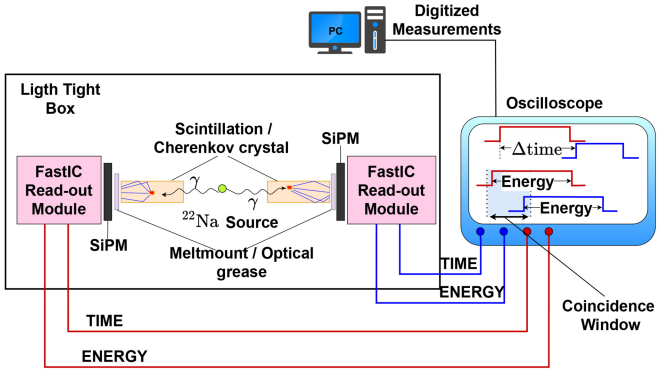

Fig. 5. Schematic representation of the experimental setup for gamma coincidence measurements.

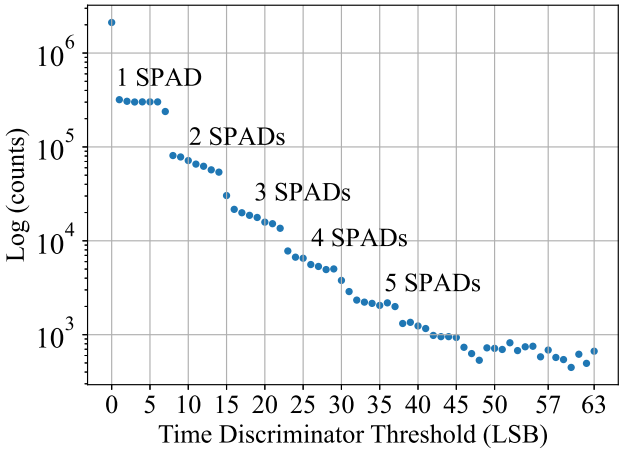

Fig. 6. Stair-case plot obtained in dark conditions showing the correlation between signal level and threshold for the time discriminator.

is obtained from the logic OR between the time signals from all the channels (which corresponds to a single channel since only one SiPM is connected). The energy is obtained from the individual output per channel. In the scope, a 25 ns time coincidence window was set between both the energy signals (Fig. 5). All the measurements were taken in a light-tight box with the temperature stabilized at 18 °C and were saved in the PC for the offline analysis.

Furthermore, a rate vs threshold scan (see Fig. 6) was performed under dark conditions for each SiPM connected to the FastIC board to determine the time threshold registers associated with different signal levels, such as single SPAD events, two SPAD events, and so forth. The time threshold comparator was set at the single SPAD signal level for all the measurements, while the internal trigger comparator was set to its maximum value to mitigate dark count interference.

Only gamma events with a measured energy within $[\mu - 0.5\sigma, \mu + \sigma]$ (with μ and σ the mean value and the standard deviation of the photopeak) were accepted. When a symmetrical $1\sigma_\mu$ range was applied, the CTR only degraded by a few picoseconds, falling within the margin of uncertainty. Finally, the resulting time delay distribution was fitted to a Gaussian function and the CTR was determined as the FWHM of the Gaussian fit.

Small scintillator crystals of size $2 \times 2 \times 3$ mm^3 were used to study the time resolution limits of the FastIC. Additionally, CTR was investigated with crystals of different sizes, with a focus on 20 mm long crystals similar to those used in the commercial TOF-PET systems. A comparative study of the time resolution of crystals from different manufacturers was conducted. To perform this evaluation, a setup similar to the one shown in Fig. 5 was used. In this case, one detector was composed of LSO:Ce:0.2%Ca measuring $2 \times 2 \times 3$ mm^3 while the other detector had the crystal under study. This detector had a detector time resolution (DTR $=$ CTR$/\sqrt{2}$) of 67 $\pm$ 3 ps. Both the crystals were coupled to HPK S13360-3050PE SiPMs using Meltmount. Therefore, any differences in time resolution between the crystals can be attributed to their intrinsic timing properties (see Table I).

C. Time Resolution Using Pure Cherenkov Radiators

In this case, an LSO:Ce:0.2%Ca crystal measuring $2 \times 2 \times 5$ mm^3 coupled with BC-630 grease to an HPK S13360-3050CS SiPM was used as a reference detector. This reference detector had a DTR of 78 $\pm$ 3 ps. Both the Cherenkov radiator and the LSO:Ce:0.2%Ca crystal were wrapped in Teflon to maximize light collection. Signal acquisition was conducted similarly to that of scintillator detectors. In these measurements, the internal trigger discriminator threshold was set at the two SPAD signal level for the Cherenkov detector to reduce the rate of accidental triggers caused by dark counts. The time discriminator threshold for the reference detector and Cherenkov detector was set to the single SPAD signal level for the optimal time measurement.

The same energy window was applied to the reference detector spectra, discarding all the events with measured energies out of the range $[\mu - 0.5\sigma, \mu + \sigma]$. Then, another energy window was applied to the Cherenkov detector spectra to select the desired events. The time distribution obtained by selecting these events was fitted to an exponentially modified Gaussian function that accounts for the characteristic long tail that appears in this detector. This tail is caused by photons that arrive later due to reflections in the back and sides of the crystal [19].

IV. FastIC Performance Evaluation

Building upon the previous findings [47], we delve into specific aspects of the FastIC performance. First, we discuss the results related to energy resolution. Subsequently, we compare the performance of FastIC with respect to HRFlexToT across a wide range of overvoltages. Then, we present detailed CTR measurements using various types and lengths of scintillators. Finally, an evaluation of FastIC readout with the Cherenkov radiators is presented.

A. Energy Resolution

Fig. 7 shows the energy spectrum of the ^{22}Na radiation source after calibration. The detector consisted of an LYSO:Ce:0.2%Ca crystal of size $3.13 \times 3.13 \times 20$ mm^3 coupled to an HPK S13360-3050PE SiPM and read by FastIC. SiPM was biased at 3 V of overvoltage. In this measurement,

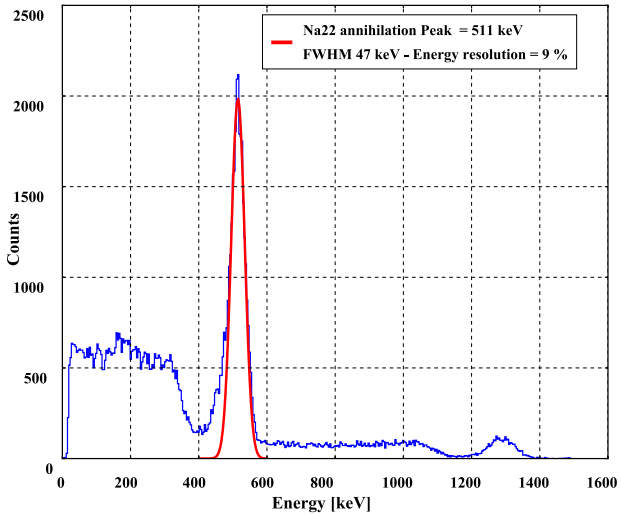

Fig. 7. Energy spectra obtained from ^{22}Na after calibration. The red line represents the Gaussian fit applied to the 511 keV photopeak. A LYSO:Ce:0.2%Ca crystal of 3.13 × 3.13 × 20 mm^3 was coupled to HPK S13360-3050PE SiPM, which was biased at 3 V of overvoltage. This measurement was performed using the energy path (linear ToT) of the FastIC.

only the energy signal from the FastIC output was recorded. This allows for a linear ToT measurement of the SiPM signal amplitude. In Fig. 7, the two characteristics peaks can be seen from ^{22}Na decay, one at 511 keV corresponding to the gamma photon emitted after the positron annihilation and another one at 1.27 MeV corresponding to the gamma photon emmitted by the ^{22}Ne unstable state. Compton edges from each gamma photon can also be appreciated. The assessed energy resolution was 9 % FWHM at 511 keV.

B. CTR Performance of the FastIC versus HRFlexToT

In Fig. 8, the performance of FastIC over a wide range of overvoltages was compared to the HRFlexToT [14] when both were connected to the HPK S13360-3050CS coupled to LSO:Ce:0.2%Ca crystals measuring $2 \times 2 \times 5$ mm^3. The crystals were coupled to the SiPMs using the Saint Gobain BC-630 optical grease. With both electronics, the CTR improves with the SiPM overvoltage up to 6 V, reaching a plateau thereafter. HRFlexToT achieved a minimum CTR of 120 ± 3 ps at 8 V of overvoltage, while FastIC yielded a minimum CTR of 107 ± 3 ps at 7 V overvoltage, representing an improvement of around ≈ 11%.

C. CTR Performance Using Different Scintillators

This section presents the CTR performance of FastIC when coupled with various combinations of SiPMs and scintillators.

1) Timing Perfomance With Short Crystals: Fig. 9 displays the CTR measurement for the FBK NUV-HD LF2 M0 coupled to the LSO:Ce:0.2%Ca crystals measuring 2 × 2 × 3 mm^3 using Meltmount. In this measurement, the overvoltage was set at 6.1 V and the time discriminator threshold was at the single SPAD signal level. Fig. 9(a) and (b) present the energy spectra for each detector. The 511 keV photopeak corresponds to pulse widths of ∼ 270 ns. The Compton edge is found at the pulse widths of ∼250 ns. We attribute the peak at the

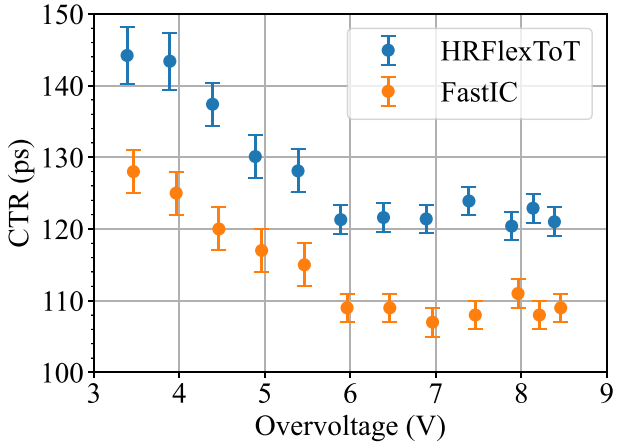

Fig. 8. Measured CTR as a function of SiPM's overvoltage for HRFlextot and FastIC. For both ASICs the same LSO:Ce:0.2%Ca crystals measuring 2×2×5 mm^3 and HPK S13360-3050CS SiPMs were employed.

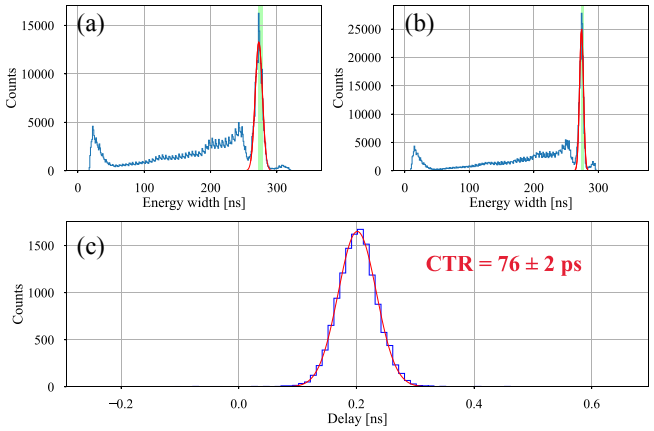

Fig. 9. CTR measurement with LSO:Ce:0.2%Ca measuring 2×2×3 mm^3 coupled to FBK NUV-HD LF2 M0 SiPM at 6.1 V of overvoltage.

low pulse widths (below 50 ns) to a combination of dark counts and optical crosstalk. Additionally, another peak can be observed in both the spectra toward the end of the spectra, with a width value larger than the photopeak. This peak appears due to the 1.27 MeV gamma photon corresponding to the ^{22}Ne unstable state. In Fig. 9(c), the time distribution of the events resulting from the acceptance energy window (see Section III-B) is shown. These acceptance windows are shown in green in Fig. 9(a) and (b). Additionally, the computed CTR is displayed, being 76 ± 2 ps.

A CTR of 95 ± 3 ps was obtained when using the HPK S13360-3050PE SiPMs, as illustrated in Fig. 10(c). Fig. 10(a) and (b) present the energy spectra of the sodium source. In this measurement, the peak caused by a mix of dark counts and crosstalk does not appears. This discrepancy may be attributed to the fact that we employed a higher threshold in the trigger detector compared to the configuration with the FBK NUV-HD LF2 M0 SiPMs, resulting in the exclusion of these events. The employment of a higher threshold arose due to a constraint in FastIC: the same register controls the step size of both the trigger and time discriminator thresholds in FastIC. Given that the FBK NUV-HD LF2 M0 SiPMs produce

TABLE III
CTR WAS MEASURED FOR VARIOUS SIPMS WHEN COUPLED TO AN LSO:CE:0.2%CA FROM AGILE OR LYSO:CE CRYSTAL FROM CPI, BOTH MEASURING $2 \times 2 \times 3$ MM^3, EACH OPERATING AT ITS OPTIMAL OVERVOLTAGE SETTING

SiPM	LSO:Ce:0.2%Ca 2x2x3 mm^3 CTR (ps) [overvoltage (V)]	LYSO:Ce 2x2x3 mm^3 CTR (ps) [overvoltage (V)]
FBK NUV-HD LF2 M0	76 ± 2 [6.1]	95 ± 3 [6.0]
FBK NUV-HD LF2 NM	82 ± 5 [6.1]	-
FBK NUV-HD-MT LF M0	-	94 ± 3 [17.0]
HPK S13360-3050VE	95 ± 3 [7.0]	-
HPK S14160-3050HS	96 ± 3 [4.5]	-
HPK S13360-3050PE	95 ± 3 [8.0]	-

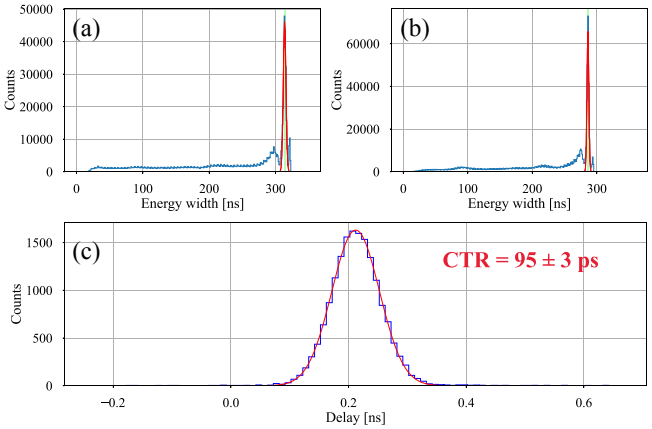

Fig. 10. CTR measurement with LSO:Ce:0.2%Ca measuring $2 \times 2 \times 3$ mm^3 coupled to HPK S13360-3050PE SiPM at 8 V of overvoltage.

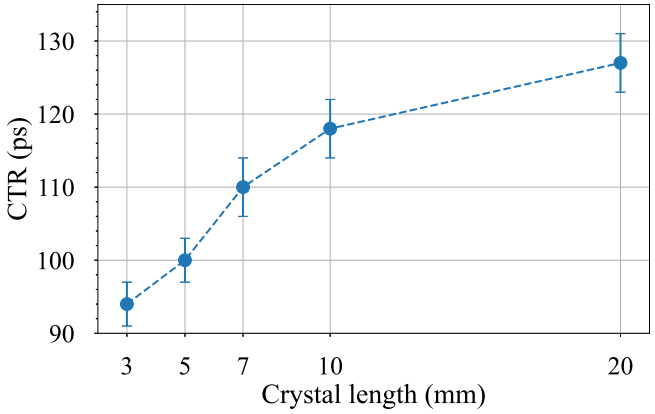

Fig. 11. Measured CTR for different crystal lengths using FBK NUV-HD LF2 M0 SiPMs. The crystals used were LYSO:Ce:0.2%Ca with sections of 3.13×3.13 mm^2.

smaller single-photon signals, we had to make adjustments to the step value used in the time discriminator threshold for these SiPMs. Consequently, these adjustments changed the maximum value at which the trigger discriminator threshold could be set, being lower for the case of FBK SiPMs.

In Table III, we present the achieved CTR for different sensors, along with the corresponding overvoltage settings for each SiPM. In general we found better results with the LSO:Ce:0.2%Ca crystal than with the LYSO:Ce one. This can be attributed to the superior time constants exhibited by the former crystal when compared to the latter (see Table I). This is already reported in [18]. Another point is that we have found better results with the new FBK sensors in comparison to the Hamamatsu sensors. This advancement enables achieving a CTR below 80 ps for the FBK NUV-HD LF2 M0 SiPM. This reduction in CTR can be attributed to the lower intrinsic SPTR performance of the FBK SiPMs (see Table II) [28]. Additionally, the FBK NUV-HD LF M0 SiPM appears to yield similar results than the FBK NUV-HD LF NM SiPM. This is in accordance with results reported in [28]. Finally, the FBK NUV-HD LF MT provides a similar time resolution to the FBK NUV-HD LF2 M0 when using an LYSO:Ce crystal. Note that, the operating overvoltage of the MT SiPM could be extended up to 18 V excess bias voltage due to its much lower crosstalk. In the case of Hamamatsu SiPMs, all the three yield similar time resolution, with the CTR being around 95 ps. This suggest that the use of TSV in HPK S13360-3050VE and HPK S14160-3050HS sensors does not degrade the CTR performance.

2) CTR Using LYSO:Ce:%0.2Ca of Different Lengths: CTR measurements for the LYSO:Ce:0.2%Ca crystals of different lengths coupled to the FBK NUV-HD LF2 M0 SiPM through Meltmount are presented in Fig. 11. The crystals had a cross section of 3.13×3.13 mm^2. The best overvoltage setting was employed for each case. As expected and as it was shown in [50], the CTR increases with the crystal length. This phenomenon arises from the fact that as the crystal length increases, the DOI and travel time spread of the optical photons exert a larger impact on the CTR [19]. Furthermore, as the crystal length increases, the LTE deteriorates leading to a reduction in the number of photons reaching the photodetector [51]. The asymptotic behavior is induced by the gamma interaction probability, which decays exponentially from the entrance of the crystal until the interaction length of approximately 12 mm [50].

Figs. 12 and 13 depict the CTR measurements for the LYSO:Ce:0.2%Ca crystal measuring $3.13 \times 3.13 \times 20$ mm^3, when coupled to the FBK NUV-HD LF2 M0 SiPM and the HPK S13360-3050PE SiPM, respectively. Upon comparing both the measurements, it can be deduced that the FBK NUV-HD LF2 M0 SiPM outperforms the HPK S13360-3050PE in terms of time resolution, which is consistent with the measurements of the LSO:Ce:0.2%Ca crystal of size $2 \times 2 \times 3$ mm^3.

3) Performance Evaluation of Scintillators From Various Manufacturers: In Table IV, we present the CTR results obtained using the LYSO crystals from different manufacturers. The variations in CTR between these measurements are

TABLE IV
COMPARISON OF DIFFERENT LYSO CRYSTALS OF COMMERCIAL SIZE USING A REFERENCE DETECTOR WITH A LSO:CE:0.2%CA OF SIZE $2 \times 2 \times 3$ MM^3. THE SIPMS USED WERE THE HPK S13360-3050PE

Crystal (Manufacturer)	Size (mm^3)	CTR ($\pm$ 4 ps FWHM)
LYSO:Ce:0.2%Ca (Crystal Photonics)	$3.13 \times 3.13 \times 20$	120
LYSO:Ce (Saint-Gobain)	$3 \times 3 \times 20$	120
LYSO:Ce (EPIC)	$3 \times 3 \times 20$	125

TABLE V
CTR PERFORMANCE AND FRACTION OF EMPLOYED EVENTS WITH RESPECT TO THE TOTAL NUMBER OF ACQUIRED EVENTS FOR DIFFERENT ENERGY WINDOWS

Crystal [Size (mm^3)]	Energy window	CTR (ps FWHM)	Fraction of events employed (%)
LSO:Ce:0.2Ca [2x2x3]	[μ-0.5σ, μ+σ]	76 $\pm$ 2	1,9
	[μ-σ, μ+σ]	77 $\pm$ 2	3.0
	(FWHM)[μ-1.18σ, μ+1.18σ]	78 $\pm$ 2	3.7
	[μ-1.5σ, μ+2σ]	79 $\pm$ 2	5.0
	[μ-1.5σ, μ+5σ]	79 $\pm$ 2	5.3
	[μ-2σ, μ+2σ]	79 $\pm$ 2	5.6
	(FWTM[a]) [μ-2.15σ, μ+2.15σ]	80 $\pm$ 2	5.8
	[μ-3σ, μ+3σ]	80 $\pm$ 2	6.3
LYSO:Ce:0.2Ca [3.13x3.13x20]	[μ-0.5σ, μ+σ]	127 $\pm$ 4	2.9
	[μ-σ, μ+σ]	130 $\pm$ 4	4.5
	(FWHM)[μ-1.18σ, μ+1.18σ]	130 $\pm$ 4	5.2
	[μ-1.5σ, μ+2σ]	129 $\pm$ 4	7.1
	[μ-1.5σ, μ+5σ]	129 $\pm$ 4	7.5
	[μ-2σ, μ+2σ]	131 $\pm$ 4	8.1
	(FWTM[a]) [μ-2.15σ, μ+2.15σ]	130 $\pm$ 4	8.5
	[μ-3σ, μ+3σ]	131 $\pm$ 4	9.3

[a] The FWTM stands for the full width tenth maximum.

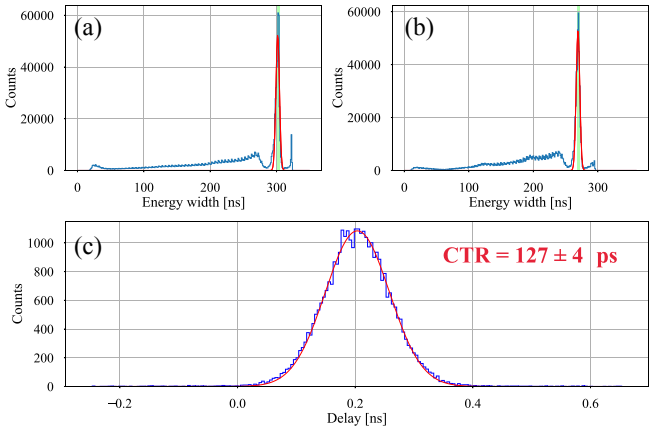

Fig. 12. CTR measurement with LSO:Ce:0.2%Ca measuring 3.12×3.12×20 mm^3 coupled to FBK NUV-HD LF2 M0 SiPM at 8.1 V of overvoltage.

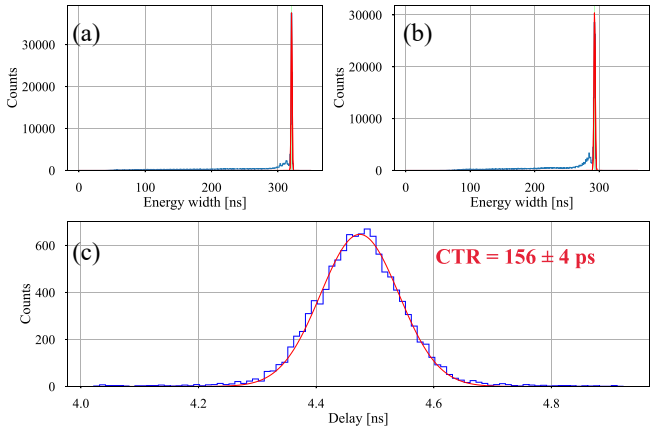

Fig. 13. CTR measurement with LSO:Ce:0.2%Ca measuring 3.12×3.12×20 mm^3 coupled to FBK NUV-HD LF2 M0 SiPM at 9 V of overvoltage.

attributable to the contribution of the LYSO crystal, as the reference detector remained constant. The LYSO:Ce crystal, measuring $3 \times 3 \times 20$ mm^3 from EPIC, achieved a time resolution of 125 $\pm$ 4 ps. Meanwhile, using a similar-sized LYSO:Ce crystal from Saint-Gobain resulted in a CTR of 120 $\pm$ 4 ps. Similarly, the LYSO:Ce:0.2%Ca crystal, sized at $3.13 \times 3.13 \times 20$ mm^3 from crystal photonics, also exhibited a CTR of 120 $\pm$ 4 ps. Consequently, all the three crystals demonstrated comparable timing performances and no significant difference was found between them.

D. Effects of the Energy Window Selection on the Time Resolution

As previously detailed in Section III, only events with measured energies within the range [$\mu - 0.5\sigma$, $\mu + \sigma$] (where μ represents the mean value and σ denotes the standard deviation of the photopeak) were selected for all the data analysis to demonstrate the ASIC's performance within a systematic energy window. Table V displays the achieved CTR when varying the energy window for the LSO:Ce:0.2%Ca crystals measuring $2 \times 2 \times 3$ mm^3 and LYSO:Ce:0.2%Ca crystals measuring $3.13 \times 3.13 \times 20$ mm^3, both connected to the FBK NUV-HD LF2 M0 SiPMs. All the measurements employs the FBK NUV-HD LF2 M0 SiPMs and at least 20K events were employed to compute the CTR.

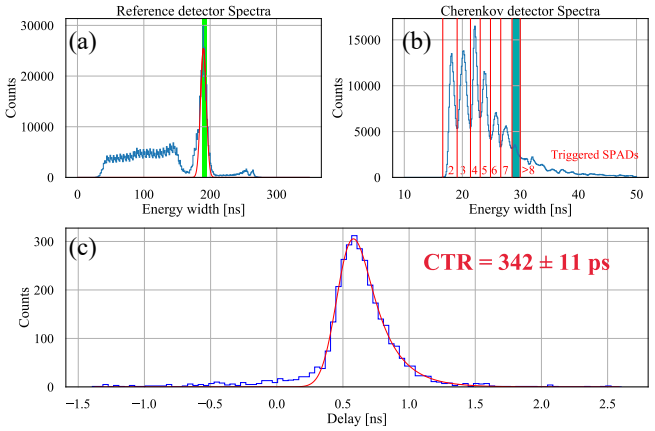

Fig. 14. Measured CTR between the reference and the Cherenkov detector. (a) and (b) Shows the energy spectra for the reference and Cherenkov detector, respectively. (c) Displays the time distribution of the detected delay times with the Gaussian fitted function.

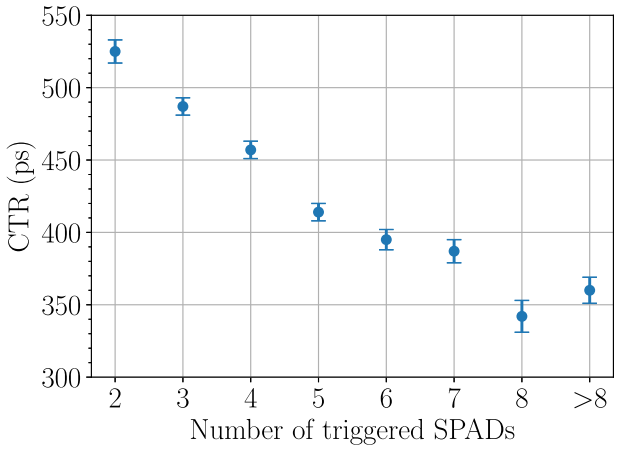

Fig. 15. CTR as a function of the number of triggered SPADs for the Cherenkov detector.

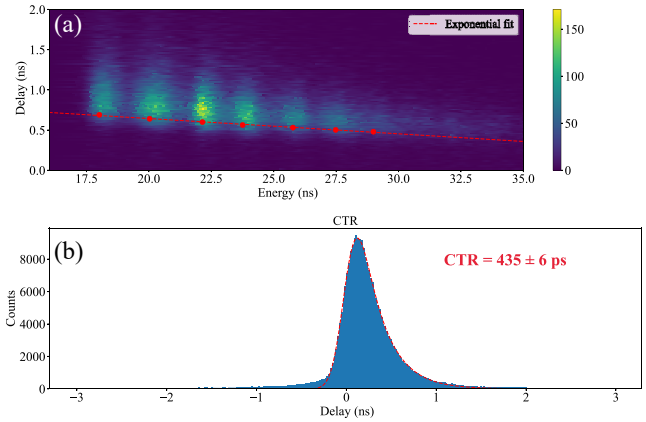

Fig. 16. (a) 2-D histogram of ToA and energy width with the fitted function shown, as well as the points used for the fitting. (b) Time distribution after time walk correction when using all event recorded in the Cherenkov detector.

A minor degradation in CTR is observed when expanding the energy window from 1σ to 3σ from the mean photopeak value, while the fraction of employed coincidence events increases by a factor of 2. Furthermore, expanding the selected window toward the higher-energy side of the photopeak enhances the sensitivity without degrading the time performance, aligning with expectations [18]. Finally, a larger fraction of detected events is observed for larger crystals, as expected due to the increased crystal longitude, which increases the probability of interaction between the gamma photon and the crystal.

E. CTR Perfomance Using Pure Cherenkov Radiators

In Fig. 14, we present the CTR measurement using a TlCl crystal measuring $3 \times 3 \times 5$ mm^3, coupled to the HPK S13360-3050CS. This measurement was conducted with an overvoltage of 5 V, and the FastIC time discriminator threshold was set at the level of a single SPAD signal. In Fig. 14(a), the energy spectra recorded by the reference detector can be seen. Fig. 14(b) displays the energy spectra recorded by the Cherenkov detector when selecting coincidences detections with the 511 keV events detected by the reference detector, as highlighted with the green window in Fig. 14(a). The peaks corresponding to events from 2 to 8 triggered SPADs can be clearly identified. Events with 0 triggered SPADs have a nonzero energy width. This is due to the fact that the pedestal of the energy signal was not subtracted. This minimum energy value in absence of an event is designed to be used to calibrate channel to channel variations, as explained in Section II. In Fig. 14(c), we show the time distribution of events corresponding to eight triggered SPADs, as highlighted in the blue window in Fig. 14(b), resulting in a CTR of 340 ± 11 ps. Finally, in Fig. 15, the CTR obtained when selecting the events for each number of triggered SPADs is presented. This curve exhibits the same traits as those reported for TlCl in [21] and for TlBr in [22], a pure Cherenkov emitter with very similar properties.

Looking at the coincidence time delay as function of the number of triggered SPADs shown in Fig. 16(a), time walk effects can be observed. This time walk arises from the fact, that the signal slope generated by the SiPM increases with the number of triggered SPADs. Since, the FastIC uses a leading-edge comparator, events with higher number of fired SPADs cross the threshold at shorter times. This behavior is well understood and has been previously reported with laser measurements [7], sole Cherenkov radiators [19], and also for a mixture of Cherenkov radiation and standard scintillation [52]. To correct the time walk, the CTR and the mean measured energy for the different peaks in the energy spectra were calculated, obtaining one point for each number of triggered SPADs [red points in Fig. 16(a)]. An exponential function was fitted to these points [red dashed line in Fig. 16(a)]. Using this exponential fitted function to correct the time walk allowed to significantly improve the measured CTR in terms of FWHM from 520 ± 5 to 435 ± 6 ps when using all the events recorded in the Cherenkov detector [Fig. 16(b)]. Furthermore, the CTR decreased from 431 ± 7 to 387 ± 7 ps after time walk correction (Fig. 17), when using a narrower event selection window in the Cherenkov energy spectra [from a minimum of six triggered SPADs and beyond Fig. 17(c)].

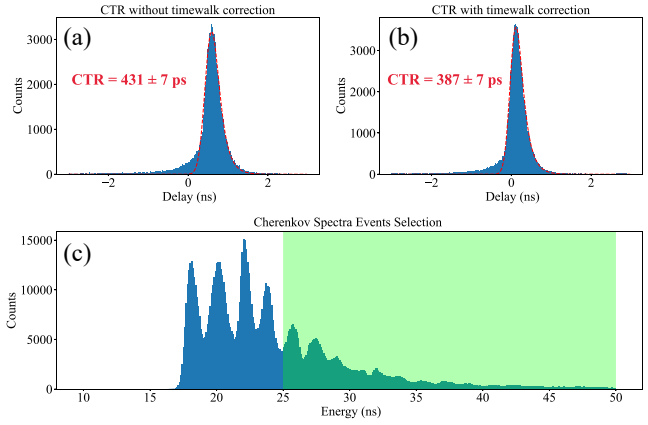

Fig. 17. (a) Time distribution without time walk correction. (b) Time distribution after time walk correction c) Energy spectra recorded by Cherenkov detector when selecting in coincidence the 511 keV events. The green window shows the events selected for the computation of the time distributions showed in (a) and (b).

V. Discussion

The new multipurpose FastIC ASIC has demonstrated excellent timing and energy resolution, with a power consumption per channel on the order of $\approx$ 12 mW. When utilizing FastIC, a CTR below 100 ps can be achieved for the short crystals, approaching 70 ps for a short LSO:Ce:0.2%Ca crystal of 2 $\times$ 2 $\times$ 3 mm^3 coupled to the FBK NUV-HD LF2 M0 SiPMs. The use of FastIC in combination with these new SiPMs demonstrates impressive timing resolution even for the 20 mm long LYSO crystals, providing a CTR below 130 ps. In this regard, the results indicate that the LYSO crystals from different manufacturers yield similar time resolution. Additionally, we have demonstrated that the FastIC can process pulses generated by prompt photons produced by the Cherenkov radiators.

The best CTR obtained using FastIC was 76 $\pm$ 2 ps. This is close to the CTR of 60 $\pm$ 3 ps obtained in [18] for the same LSO:Ce:0.2%Ca crystal of 2 $\times$ 2 $\times$ 3 mm^3 crystal coupled to the previous FBK SiPM technology (NUV-HD), connected to an HF front-end electronic and digitized using a fast oscilloscope [39] (Table VI). The timing performance degraded to 127 $\pm$ 4 ps for a LYSO:Ce:0.2%Ca crystal measuring 3.13 $\times$ 3.13 $\times$ 20 mm^3 coupled to the FBK NUV-HD LF2 M0. This behavior was expected, as DOI and optical travel transfer effects have a bigger impact on the timing resolution when increasing the crystal length [50]. Measurements performed with the HF electronics and digitized with a fast oscilloscope yielded a CTR of 107 $\pm$ 3 ps for an LYSO:Ce:0.2%Ca crystal of 3 $\times$ 3 $\times$ 20 mm^3 coupled to the FBK NUV-HD LF2 M0 [28].

The performance difference between both the electronics could arise from various sources. One possible explanation could be that the HF has lower electronic noise ($\sigma_{\text{elec.noise}}$) than the FastIC. This implies that the HF may have a lower electronic jitter contribution, as this contribution scales as $\sigma_{\text{elec.noise}}$/SR. Another explanation could be attributed to the electronics bandwidth. A low bandwidth may affect the rising edge of the SiPM's signal, subsequently impacting the SR of the signal. HF has a 1.5 GHz bandwidth [39], whereas FastIC has a bandwidth in the order of hundred's of MHz. Although, the effective bandwidth also depends on the parasitic inductance and SiPM's capacitance [15], and thus the differences in the electronics bandwidth could be less significant. Additionally, the setup with the HF electronics and a fast oscilloscope features an ideal comparator in the sense that the ToA is extracted through an offline leading edge comparator algorithm after measuring the analog response of the SiPM with an oscilloscope. This differs from FastIC, which includes a current comparator on-chip that affects the time response, i.e., it adds jitter to the measurement (see Fig. 1).

In Table VI, a comparison of the performance demonstrated by several ASICs for fast-timing applications and the HF electronics measured by other groups is presented. In this work, we demonstrated that with the FastIC we could improve the CTR with respect to its predecessor, HRFlexToT, by $\approx$11%. It is worth noting that the HRFlexToT consumes only $\approx$ 3.5 mW/ch compared to the $\approx$ 12 mW/ch of the FastIC. The FastIC has a larger power consumption for several reasons. First, it provides a differential output, whereas the HRFlexToT has a single-ended output. The differential transmission has a larger power consumption, but it improves the signal integrity due to lower crosstalk in the signal transmission path. Moreover, the FastIC is a multipurpose ASIC capable of processing fast short pulses of a few ns FWHM, which is typical of PMTs, and thus requiring more power to have a larger bandwidth in the energy processing chain. In contrast, the HRFlexToT is specifically designed for PET applications. Therefore, the power consumption of the FastIC could be optimized if it were modified to work exclusively for PET applications. Finally, a common advantage of both the ASICs compared to the HF electronics is that the time and energy information are encoded in a single processing channel, whereas in the HF electronics, energy and time are processed separately, requiring twice the resources.

Recent measurements with Radioroc ASIC from Weeroc demonstrated a CTR of $\approx$ 83 ps when using the LYSO:Ce:0.2%Ca crystals measuring 2 $\times$ 2 $\times$ 3 mm^3 coupled to the Broadcom NUV-MT SiPMs, and $\approx$127 ps when extending the size of the LYSO crystal to 3 $\times$ 3 $\times$ 20 mm^3. Although both the crystals and SiPMs in this measurement differed from those employed for the evaluation of the FastIC ASIC, their performance was rather similar, allowing for a fair comparison between the ASICs. However, the performance of FastIC using a 20 mm long LYSO crystal could be deteriorated due to a potential loss of light, as the dimensions of the crystal section (3.13 $\times$ 3.13 mm^2) are similar to those of the SiPM (3.12 $\times$ 3.2 mm^2).

Table VI also details that the FastIC outperforms the well-known TOF-PET ASIC called TOFPET2, designed by PETsys electronics. However, TOFPET2 includes an internal TDC for data digitization, while FastIC requires an external TDC implemented in an FPGA to build a system (or an oscilloscope for the experimental evaluation). The usage of an external FPGA-based TDC to build a complete detector module was successfully studied with the HRFlexToT [53] and FastIC [54].

TABLE VI
STATE OF THE ART OF DIFFERENT ASICS SUITABLE FOR TOF-PET APPLICATIONS. THE HF READOUT IS ALSO SHOWN TO ILLUSTRATE THE TIME RESOLUTION LIMITS THAT CAN BE ACHIEVED

ASIC	Power (mW/channel)	Crystal (Producer) size(mm^3)	SiPM [size(mm^2)]	Data acquisition method[e]	CTR (ps)	Reference
TOFPET2	8.2	LYSO:Ce:Ca (TAC) 3×3×19	Broadcom NUV-MT [3.8×3.8]	TDC ≈ 20 ps [a]	157 ± 1	[55], [51]
HRFlexToT	3.5	LSO:Ce:Ca (AGILE) 2×2×5	HPK S13360-3050CS [3×3]	Oscilloscope	120 ± 3	This work
HF readout	720	LSO:Ce:Ca (AGILE) 2×2×3	FBK NUV-HD [4×4]	Oscilloscope + ideal comparator	60 ± 3	[18]
HF readout	143	LYSO:Ce:Ca (TAC) 3×3×20	FBK NUV-HD LF2 M0 [3×3]	Oscilloscope + ideal comparator	107 ± 3	[28]
HF readout	143	LYSO:Ce:Ca (TAC) 2×2×3	Broadcom NUV-MT [3.8×3.8]	Oscilloscope + ideal comparator	56 ± 2	[55]
HF readout	143	LYSO:Ce:Ca (TAC) 3×3×19	Broadcom NUV-MT [3.8×3.8]	Oscilloscope + ideal comparator	95 ± 2	[55]
Radioroc	-[b]	LYSO:Ce:Ca (TAC) 2×2×3	Broadcom NUV-MT [4×4]	Oscilloscope	83 ± 3	[31], [56]
Radioroc	-[b]	LYSO:Ce:Ca (TAC) 3×3×20	Broadcom NUV-MT [4×4]	Oscilloscope	127 ± 3	[31], [56]
FastIC	12	LSO:Ce:Ca (Agile) 2×2×3	FBK NUV-HD LF2 M0 [3.12×3.2]	Oscilloscope	76 ± 2	This work
FastIC	12	LYSO:Ce:Ca (CPI) 3.13×3.13×20	FBK NUV-HD LF2 M0 [3.12×3.2]	Oscilloscope	127 ± 2	This work
FastIC	12	LSO:Ce:Ca (AGILE) 2×2×5	HPK S13360-3050CS [3×3]	Oscilloscope	107 ± 3	This work
FastIC	12	LYSO:Ce:Ca (CPI) 3.13×3.13×20	HPK S13360-3050PE [3×3]	Oscilloscope	156 ± 4	This work
FastIC+	12.5	LSO:Ce:Ca (AGILE) 2×2×3	FBK NUV-HD LF2 M0 [3.12×3.2]	TDC ≈ 22 ps [c]	≈ 87[d]	Estimated
FastIC+	12.5	LYSO:Ce:Ca (CPI) 3.13×3.13×20	FBK NUV-HD LF2 M0 [3.12×3.2]	TDC ≈ 22 ps[c]	≈ 134[d]	Estimated

[a] This is the expected jitter (in FWHM) obtained using the following equation: $\text{TDC}_{jitter}=2.35 \cdot (\text{Time}_{bin}/\sqrt{(12)})$.
[b] Power consumption has not been disclosed yet. Its predecessor, the Citiroc, has a power consumption of 7 mW per channel.
[c] Simulated jitter was obtained based on transient simulations of the entire TDC readout.
[d] This is a theoretical number obtained by adding quadratically the contribution of the analog part and the digital part, i.e., $\text{CTR}_{\text{total}}=\sqrt{\text{CTR}^2_{\text{analog}}+\text{CTR}^2_{\text{TDC}}}$. $\text{CTR}_{\text{analog}}$ is the correspondent measured value.
[e] Note that HF readout outputs an analog signal, and an ideal comparator is used to measure the CTR. The rest of the electronics in the table, i.e, all ASICs, include an internal comparator to obtain the timestamp, which outputs a binary signal that can be acquired either by an oscilloscope or by a TDC.

Therefore, this proves the scalability of the FastIC for building a system, despite not having an internal TDC.

New FBK SiPMs allow to achieve a lower CTR compared to the HPK sensors, thanks to an improved SPTR performance (see Table II). In this context, the low crosstalk demonstrated by the FBK metal-trench technology enables to use a much higher overvoltage. However, applying larger overvoltages does not necessarily result in better CTR performance, which aligns with the findings presented by Merzi et al. [27]. In their study, they only saw a marginal improvement in CTR performance when substituting the FBK NUV-HD with the FBK NUV-HD-MT. Nevertheless, the FBK NUV-HD-MT LF M0 exhibited a broader minimum compared to the FBK NUV-HD LF2 M0, i.e., the best CTR performance is achieved for a larger range of overvoltages when using the MT technology [27]. This broader minimum will be advantageous for the systems with hundreds of SiPMs not having the same break-down voltage by reducing the precision needed to bias all the sensors for optimum performance. Additionally, measurements performed using the FBK SiPMs without a mask (FBK NUV-HD LF2 NM) exhibit slightly similar performance to the SiPMs with mask M0. This is in accordance with Gundacker et al. [28] where they obtained similar performance for both the SiPMs when using the HF connected to the oscilloscope.

Experimental measurements show that the FastIC can detect the low light intensity generated by the pure Cherenkov radiators, being able to replicate results obtained with high-consumption readout electronics [21] with an ASIC that could be suitable for building scanners. Nevertheless, there is room for improvement in the timing performance. The surface treatment of the TlCl crystal, for example, is deemed crucial for obtaining a good time performance [20] and obtain measurements closer to those reported with the LSO/LYSO crystals.

These measurements (or in general with any other Cherenkov radiator, such as TlBr or PbF2) can be further improved by applying several strategies. First, new FBK SiPMs could be used instead of the HPK sensors, due to their better PDE and SPTR [18], [27], [28] and consequently better CTR, as shown throughout this work. Second, a source of degradation could come from the event selection. Both the noncorrelated and correlated noise sources, such as dark counts, after-pulses, and crosstalk, can lead to the accumulation of pulses (pile-up), which in turn makes event selection more challenging when considering peak amplitudes,

as explored in this work. The application of a first-order high-pass RC circuit between the SiPM and the input of the ASIC will reduce the effective FWHM of the detector response, thereby reducing pile-up effects and enabling better event selection for time walk corrections. Another strategy could involve using the rise time of the input signal to correct the time walk, as presented in [19]. However, this technique would require the implementation of a second comparator with low jitter in the ASIC to obtain a second timestamp for computing the rise time of the signal. Finally, this work demonstrated the ability of the FastIC to detect low-intensity prompt emission light, opening the possibility to enhance the BGO timing performance by detecting the Cherenkov photons produced in BGO [57].

FastIC+ will be the successor of FastIC, incorporating an integrated TDC per channel. Preliminary studies indicate that this TDC will introduce a jitter contribution of approximately ≈22 ps (FWHM) without significantly increasing the overall power consumption per channel (around 5% larger). Consequently, the TDC is expected to have a minimal effect on the time resolution compared to the FastIC, as shown in Table VI. Finally, the evaluation of FastIC at the single-pixel level shows promising results compared to the newly produced Siemens biograph vision X, which has a CTR of ≈178 ps [45]. Preliminary studies estimate a CTR of ≈134 ps for a 20 mm long crystal (see Table VI) when using the FastIC+ ASIC.

All our measurements were done with single-channel detectors, primarily aimed at identifying the time resolution limits of FastIC in comparison to the other electronics. However, time resolution will degrade when testing detectors with a larger number of channels. This degradation is caused by intercrystals crosstalk, optical crosstalk from SiPM, and light sharing due to the coupling material [58]. Internal crosstalk within the ASIC has been measured as negligible by injecting an electrical signal in one channel and detecting negligible signal in adjacent channels. Further measurements involving the detector arrays remain a topic for future research. A thorough evaluation of the FastIC+ with single and multiple channels is a topic for future work.

VI. Conclusion

To achieve a sub-100 ps TOF-PET scanner, significant advancements are required in read-out electronics, all while maintaining low power consumption, a compact form factor, and cost-effectiveness. The newly developed versatile read-out ASIC, known as FastIC, demonstrates low power consumption (≈ 12 mW) per channel and the capability to achieve remarkable results in terms of timing performance and energy resolution. Specifically, a CTR of 76±2 ps was achieved when employing the FBK NUV-HD L2 M0 SiPMs in conjunction with the LSO:Ce:0.2%Ca crystals measuring $2 \times 2 \times 3$ mm^3. For larger clinical-scale crystals ($3.13 \times 3.13 \times 20$ mm^3), a CTR of 127 ± 4 was obtained using the LYSO:Ce:0.2%Ca crystals produced by Crystal Photonics Inc. The energy resolution obtained when the same LYSO:Ce:0.2%Ca crystal was coupled to the HPK S13360-3050PE SiPM was 9%. In addition to these achievements, the evaluation of the TlCl pure Cherenkov emitter demonstrated the ability to detect low-light events with a time resolution comparable to those reported in the literature using HF electronics.

An upcoming version of the ASIC, known as FastIC+, will integrate a TDC with a time jitter of ≈ 22 ps FWHM. Further exploration into 2.5D/3-D integration is planned to reduce the effects of interconnection parasitics between the ASIC and the sensor.

Acknowledgment

The authors would like to express their gratitude to Alberto Gola and his group (FBK, Italy) for providing the SiPM samples and engaging in fruitful discussions. Additionally, they extend their thanks to Rok Pestonik (JSI, Slovenia) for providing the LYSO crystals from Crystal Photonics Inc., and for the valuable discussions. Finally, we thank Bruce Chai from Crystal Photonics Inc., for providing an small size LYSO sample for the measurements and RMD Inc., for providing the TlCl crystal.

All the authors declare that they have no known conflicts of interest in terms of competing financial interests or personal relationships that could have an influence or are relevant to the work reported in this article.

References

[1] M. Conti and B. Bendriem, "The new opportunities for high time resolution clinical TOF PET," *Clin. Transl. Imag.*, vol. 7, no. 2, pp. 139–147, Apr. 2019. [Online]. Available: http://link.springer.com/10.1007/s40336-019-00316-5

[2] S. Surti, "Update on time-of-flight PET imaging," *J. Nucl. Med.*, vol. 56, no. 1, pp. 98–105, Jan. 2015. [Online]. Available: http://jnm.snmjournals.org/lookup/doi/10.2967/jnumed.114.145029

[3] S. Vandenberghe, E. Mikhaylova, E. D'Hoe, P. Mollet, and J. S. Karp, "Recent developments in time-of-flight PET," *EJNMMI Phys.*, vol. 3, no. 1, pp. 1–30, Dec. 2016. [Online]. Available: https://ejnmmiphys.springeropen.com/articles/10.1186/s40658-016-0138-3

[4] D. R. Schaart, "Physics and technology of time-of-flight PET detectors," *Phys. Med. Biology*, vol. 66, no. 9, May 2021, Art. no. 09TR01. [Online]. Available: https://iopscience.iop.org/article/10.1088/1361-6560/abee56

[5] A. Gonzalez-Montoro et al., "A new brain dedicated PET scanner with 4D detector information," *Bio-Algorithms Med.-Syst.*, vol. 18, no. 1, pp. 107–119, Dec. 2022. [Online]. Available: http://archive.sciendo.com/BIOAL/bioal.2020.18.issue-1/bioal-2022-0083/bioal-2022-0083.pdf

[6] M. Freire et al., "Experimental validation of a rodent PET scanner prototype based on a single LYSO crystal tube," *IEEE Trans. Radiat. Plasma Med. Sci.*, vol. 6, no. 6, pp. 697–706, Jul. 2022. [Online]. Available: https://ieeexplore.ieee.org/document/9596579/

[7] R. Dolenec, S. Korpar, P. Krizan, and R. Pestotnik, "SiPM timing at low light intensities," in *Proc. IEEE Nucl. Sci. Symp., Med. Imag. Conf. Room-Temp. Semicond. Detect. Workshop (NSS/MIC/RTSD)*, 2016, pp. 1–5. [Online]. Available: https://ieeexplore.ieee.org/document/8069832/

[8] A. Gola et al., "NUV-sensitive silicon photomultiplier technologies developed at Fondazione Bruno Kessler," *Sensors*, vol. 19, no. 2, p. 308, Jan. 2019. [Online]. Available: http://www.mdpi.com/1424-8220/19/2/308

[9] C. Piemonte and A. Gola, "Overview on the main parameters and technology of modern silicon photomultipliers," *Nucl. Instrum. Methods Phys. Res. Sect. A, Accelerators, Spectrometers, Detectors Assoc. Equip.*, vol. 926, pp. 2–15, May 2019. [Online]. Available: https://linkinghub.elsevier.com/retrieve/pii/S0168900218317716

[10] S. Vinogradov, "Approximations of coincidence time resolution models of scintillator detectors with leading edge discriminator," *Nucl. Instrum. Methods Phys. Res. Sect. A, Accelerators, Spectrometers, Detectors Assoc. Equip.*, vol. 912, pp. 149–153, Dec. 2018. [Online]. Available: https://linkinghub.elsevier.com/retrieve/pii/S0168900217311956

[11] S. Seifert, H. T. van Dam, and D. R. Schaart, "The lower bound on the timing resolution of scintillation detectors," *Phys. Med. Biol.*, vol. 57, no. 7, pp. 1797–1814, Apr. 2012. [Online]. Available: https://iopscience.iop.org/article/10.1088/0031-9155/57/7/1797

[12] M. Toussaint, F. Loignon-Houle, J.-P. Dussault, and R. Lecomte, "Analytical model of DOI-induced time bias in ultra-fast scintillation detectors for TOF-PET," *Phys. Med. Biol.*, vol. 64, no. 6, Mar. 2019, Art. no. 65009. [Online]. Available: https://iopscience.iop.org/article/10.1088/1361-6560/ab038b

[13] S. E. Derenzo, W.-S. Choong, and W. W. Moses, "Fundamental limits of scintillation detector timing precision," *Phys. Med. Biol.*, vol. 59, no. 13, pp. 3261–3286, Jul. 2014. [Online]. Available: https://iopscience.iop.org/article/10.1088/0031-9155/59/13/3261

[14] D. Sanchez et al., "HRFlexToT: A high dynamic range ASIC for time-of-flight positron emission tomography," *IEEE Trans. Radiat. Plasma Med. Sci.*, vol. 6, no. 1, pp. 51–67, Jan. 2022. [Online]. Available: https://ieeexplore.ieee.org/document/9380735/

[15] J. Fernandez-Tenllado, R. Ballabriga, M. Campbell, D. Gascon, S. Gomez, and J. Mauricio, "Optimal design of single-photon sensor front-end electronics for fast-timing applications," in *Proc. IEEE Nucl. Sci. Symp. Med. Imag. Conf. (NSS/MIC)*, 2019, pp. 1–5. [Online]. Available: https://ieeexplore.ieee.org/document/9059805/

[16] J. W. Cates, S. Gundacker, E. Auffray, P. Lecoq, and C. S. Levin, "Improved single photon time resolution for analog SiPMs with front end readout that reduces influence of electronic noise," *Phys. Med. Biol.*, vol. 63, no. 18, Sep. 2018, Art. no. 185022. [Online]. Available: https://iopscience.iop.org/article/10.1088/1361-6560/aadbcd

[17] D. Sánchez, S. Gómez, J. M. Fernández-Tenllado, R. Ballabriga, M. Campbell, and D. Gascón, "Multimodal simulation of large area silicon photomultipliers for time resolution optimization," *Nucl. Instrum. Methods Phys. Res. Sect. A, Accelerators, Spectrometers, Detectors Assoc. Equip.*, vol. 1001, Jun. 2021, Art. no. 165247. [Online]. Available: https://linkinghub.elsevier.com/retrieve/pii/S016890022100231X

[18] S. Gundacker et al., "Experimental time resolution limits of modern SiPMs and TOF-PET detectors exploring different scintillators and cherenkov emission," *Phys. Med. Biol.*, vol. 65, no. 2, Jan. 2020, Art. no. 25001. [Online]. Available: https://iopscience.iop.org/article/10.1088/1361-6560/ab63b4

[19] N. Kratochwil, S. Gundacker, and E. Auffray, "A roadmap for sole cherenkov radiators with SiPMs in TOF-PET," *Phys. Med. Biol.*, vol. 66, no. 19, Oct. 2021, Art. no. 195001. [Online]. Available: https://iopscience.iop.org/article/10.1088/1361-6560/ac212a

[20] G. Terragni et al., "Time resolution studies of thallium based cherenkov semiconductors," *Front. Phys.*, vol. 10, Mar. 2022, Art. no. 785627. [Online]. Available: https://www.frontiersin.org/articles/10.3389/fphy.2022.785627/full

[21] G. Arino-Estrada et al., "Study of Čerenkov light emission in the semiconductors TlBr and TlCl for TOF-PET," *IEEE Trans. Radiat. Plasma Med. Sci.*, vol. 5, no. 5, pp. 630–637, Sep. 2021. [Online]. Available: https://ieeexplore.ieee.org/document/9199281/

[22] G. Ariño-Estrada et al., "First cerenkov charge-induction (CCI) TlBr detector for TOF-PET and proton range verification," *Phys. Med. Biol.*, vol. 64, no. 17, Aug. 2019, Art. no. 175001. [Online]. Available: https://iopscience.iop.org/article/10.1088/1361-6560/ab35c4

[23] S. I. Kwon, A. Gola, A. Ferri, C. Piemonte, and S. R. Cherry, "Bismuth germanate coupled to near ultraviolet silicon photomultipliers for time-of-flight PET," *Phys. Med. Biol.*, vol. 61, no. 18, pp. L38–L47, Sep. 2016. [Online]. Available: https://iopscience.iop.org/article/10.1088/0031-9155/61/18/L38

[24] S. E. Brunner and D. R. Schaart, "BGO as a hybrid scintillator / cherenkov radiator for cost-effective time-of-flight PET," *Phys. Med. Biol.*, vol. 62, no. 11, pp. 4421–4439, Jun. 2017. [Online]. Available: https://iopscience.iop.org/article/10.1088/1361-6560/aa6a49

[25] F. Pagano, N. Kratochwil, M. Salomoni, M. Pizzichemi, M. Paganoni, and E. Auffray, "Advances in heterostructured scintillators: Toward a new generation of detectors for TOF-PET," *Phys. Med. Biol.*, vol. 67, no. 13, Jul. 2022, Art. no. 135010. [Online]. Available: https://iopscience.iop.org/article/10.1088/1361-6560/ac72ee

[26] R. M. Turtos, S. Gundacker, E. Auffray, and P. Lecoq, "Towards a metamaterial approach for fast timing in PET: Experimental proof-of-concept," *Phys. Med. Biol.*, vol. 64, no. 18, Sep. 2019, Art. no. 185018. [Online]. Available: https://iopscience.iop.org/article/10.1088/1361-6560/ab18b3

[27] S. Merzi et al., "NUV-HD SiPMs with metal-filled trenches," *J. Instrum.*, vol. 18, no. 5, May 2023, Art. no. P05040. [Online]. Available: https://iopscience.iop.org/article/10.1088/1748-0221/18/05/P05040

[28] S. Gundacker et al., "On timing-optimized SiPMs for cherenkov detection to boost low cost time-of-flight PET," *Phys. Med. Biology*, vol. 68, no. 16, Aug. 2023, Art. no. 165016. [Online]. Available: https://iopscience.iop.org/article/10.1088/1361-6560/ace8ee

[29] F. Anghinolfi et al., "NINO: An ultra-fast and low-power front-end amplifier/discriminator ASIC designed for the multigap resistive plate chamber," *Nucl. Instrum. Methods Phys. Res. Sect. A, Accelerators, Spectrometers, Detectors Assoc. Equip.*, vol. 533, nos. 1–2, pp. 183–187, Nov. 2004. [Online]. Available: https://linkinghub.elsevier.com/retrieve/pii/S0168900204014299

[30] S. Ahmad et al., "Petiroc2A: Characterization and experimental results," in *Proc. IEEE Nucl. Sci. Symp. Med. Imag. Conf. Proc. (NSS/MIC)*, 2018, pp. 1–4. [Online]. Available: https://ieeexplore.ieee.org/document/8824464/

[31] T. Saleem et al., "Study experimental time resolution limits of recent ASICs at Weeroc with different SiPMs and scintillators," *J. Instrum.*, vol. 18, no. 10, Oct. 2023, Art. no. P10005. [Online]. Available: https://iopscience.iop.org/article/10.1088/1748-0221/18/10/P10005

[32] V. Nadig, B. Weissler, H. Radermacher, V. Schulz, and D. Schug, "Investigation of the power consumption of the PETsys TOFPET2 ASIC," *IEEE Trans. Radiat. Plasma Med. Sci.*, vol. 4, no. 3, pp. 378–388, May 2020. [Online]. Available: https://ieeexplore.ieee.org/document/8908729/

[33] D. Schug, V. Nadig, B. Weissler, P. Gebhardt, and V. Schulz, "Initial measurements with the PETsys TOFPET2 ASIC evaluation kit and a characterization of the ASIC TDC," *IEEE Trans. Radiat. Plasma Med. Sci.*, vol. 3, no. 4, pp. 444–453, Jul. 2019. [Online]. Available: https://ieeexplore.ieee.org/document/8556088/

[34] "PETsys electronics." Accessed: Jun. 1, 2024. [Online]. Available: https://www.petsyselectronics.com/web/

[35] I. Sarasola et al., "A comparative study of the time performance between NINO and FlexToT ASICs," *J. Instrum.*, vol. 12, no. 4, Apr. 2017, Art. no. P04016. [Online]. Available: https://iopscience.iop.org/article/10.1088/1748-0221/12/04/P04016

[36] J. M. Cela et al., "A compact detector module design based on FlexToT ASICs for time-of-flight PET-MR," *IEEE Trans. Radiat. Plasma Med. Sci.*, vol. 2, no. 6, pp. 549–553, Nov. 2018. [Online]. Available: https://ieeexplore.ieee.org/document/8467343/

[37] A. Comerma et al., "FlexToT-current mode ASIC for readout of common cathode SiPM arrays," in *Proc. IEEE Nucl. Sci. Symp. Conf. Rec.*, 2013, pp. 1–2.

[38] J. Trenado et al., "Performance of FlexToT time based PET readout ASIC for depth of interaction measurements," in *Proc. Technol. Instrum. Part. Phys. PoS(TIPP2014)*, Trieste, Italy, 2015, p. 241. [Online]. Available: https://pos.sissa.it/213/241

[39] S. Gundacker, R. M. Turtos, E. Auffray, M. Paganoni, and P. Lecoq, "High-frequency SiPM readout advances measured coincidence time resolution limits in TOF-PET," *Phys. Med. Biol.*, vol. 64, no. 5, Feb. 2019, Art. no. 55012. [Online]. Available: https://iopscience.iop.org/article/10.1088/1361-6560/aafd52

[40] M. Krake, V. Nadig, V. Schulz, and S. Gundacker, "Power-efficient high-frequency readout concepts of SiPMs for TOF-PET and HEP," *Nucl. Instrum. Methods Phys. Res. Sect. A, Accelerators, Spectrometers, Detectors Assoc. Equip.*, vol. 1039, Sep. 2022, Art. no. 167032. [Online]. Available: https://linkinghub.elsevier.com/retrieve/pii/S0168900222004570

[41] J. W. Cates and W.-S. Choong, "Low power implementation of high frequency SiPM readout for cherenkov and scintillation detectors in TOF-PET," *Phys. Med. Biol.*, vol. 67, no. 19, Oct. 2022, Art. no. 195009. [Online]. Available: https://iopscience.iop.org/article/10.1088/1361-6560/ac8963

[42] S. Surti, A. R. Pantel, and J. S. Karp, "Total body PET: Why, how, what for?" *IEEE Trans. Radiat. Plasma Med. Sci.*, vol. 4, no. 3, pp. 283–292, May 2020. [Online]. Available: https://ieeexplore.ieee.org/document/9056798/

[43] B. A. Spencer et al., "Performance evaluation of the uEXPLORER total-body PET/CT scanner based on NEMA NU 2-2018 with additional tests to characterize PET scanners with a long axial field of view," *J. Nucl. Med.*, vol. 62, no. 6, pp. 861–870, Jun. 2021. [Online]. Available: http://jnm.snmjournals.org/lookup/doi/10.2967/jnumed.120.250597

[44] V. Nadig, K. Herrmann, F. M. Mottaghy, and V. Schulz, "Hybrid total-body pet scanners—Current status and future perspectives," *Eur. J. Nucl. Med. Mol. Imag.*, vol. 49, no. 2, pp. 445–459, Jan. 2022. [Online]. Available: https://link.springer.com/10.1007/s00259-021-05536-4

[45] (Siemens Healthineers USA, Inc., Malvern, PA, USA). *Siemens Healthineers Debuts Biograph Vision.X PET/CT Scanner*. [Online]. Available: https://www.siemens-healthineers.com/en-us/press-room/press-releases/biograph-vison-x-pet-ct-scanner-debut

[46] S. Gómez et al., "FastIC: A fast integrated circuit for the readout of high performance detectors," *J. Instrum.*, vol. 17, no. 5, May 2022, Art. no. C05027. [Online]. Available: https://iopscience.iop.org/article/10.1088/1748-0221/17/05/C05027

[47] S. Gomez et al., "FastIC: A highly configurable ASIC for fast timing applications," in *Proc. IEEE Nucl. Sci. Symp. Med. Imag. Conf. (NSS/MIC)*, 2021, pp. 1–4. [Online]. Available: https://ieeexplore.ieee.org/document/9875546/

[48] A. Gonzalez-Montoro et al., "Evolution of PET detectors and event positioning algorithms using monolithic scintillation crystals," *IEEE Trans. Radiat. Plasma Med. Sci.*, vol. 5, no. 3, pp. 282–305, May 2021. [Online]. Available: https://ieeexplore.ieee.org/document/9353691/

[49] K. K. A. Ghassemi and K. Sato (Hamamatsu, Bridgewater, NJ, USA). *A Technical Guide to Silicon Photomutlipliers MPPC Section 2*. [Online]. Available: https://hub.hamamatsu.com/us/en/technical-notes/mppc-sipms/a-technical-guide-to-silicon-photomutlipliers-MPPC-Section-2.html

[50] S. Gundacker, A. Knapitsch, E. Auffray, P. Jarron, T. Meyer, and P. Lecoq, "Time resolution deterioration with increasing crystal length in a TOF-PET system," *Nucl. Instrum. Methods Phys. Res. Sect. A: Accelerators, Spectrometers, Detectors Assoc. Equip.*, vol. 737, pp. 92–100, Feb. 2014. [Online]. Available: https://linkinghub.elsevier.com/retrieve/pii/S0168900213015647

[51] S. Gundacker et al., "State of the art timing in TOF-PET detectors with LuAG, GAGG and L(Y)SO scintillators of various sizes coupled to FBK-SiPMs," *J. Instrum.*, vol. 11, no. 8, Aug. 2016, Art. no. P08008. [Online]. Available: https://iopscience.iop.org/article/10.1088/1748-0221/11/08/P08008

[52] N. Kratochwil, S. Gundacker, P. Lecoq, and E. Auffray, "Pushing cherenkov PET with BGO via coincidence time resolution classification and correction," *Phys. Med. Biology*, vol. 65, no. 11, Jun. 2020, Art. no. 115004. [Online]. Available: https://iopscience.iop.org/article/10.1088/1361-6560/ab87f9

[53] P. Carra et al., "A neural network-based algorithm for simultaneous event positioning and timestamping in monolithic scintillators," *Phys. Med. Biol.*, vol. 67, no. 13, Jul. 2022, Art. no. 135001. [Online]. Available: https://iopscience.iop.org/article/10.1088/1361-6560/ac72f2

[54] F. Keizer, "A novel fast-timing readout chain for LHCb RICH LS3 and prototype beam tests," *Nucl. Instrum. Methods Phys. Res. Sect. A, Accelerators, Spectrometers, Detectors Assoc. Equip.*, vol. 1055, Oct. 2023, Art. no. 168475. [Online]. Available: https://linkinghub.elsevier.com/retrieve/pii/S0168900223004655

[55] V. Nadig et al., "Timing advances of commercial divalent-ion co-doped LYSO:Ce and SiPMs in sub-100 ps time-of-flight positron emission tomography," *Phys. Med. Biol.*, vol. 68, no. 7, Apr. 2023, Art. no. 75002. [Online]. Available: https://iopscience.iop.org/article/10.1088/1361-6560/acbde4

[56] G. Contino et al., "An ASIC front-end for fluorescence and cherenkov light detection with SiPM for space and ground applications," *Nucl. Instrum. Methods Phys. Res. Sect. A, Accelerators, Spectrometers, Detectors Assoc. Equip.*, vol. 980, Nov. 2020, Art. no. 164510. [Online]. Available: https://linkinghub.elsevier.com/retrieve/pii/S0168900220309074

[57] M. Piller et al., "FastIC ASIC readout performance for cherenkov based TOF-PET imaging," in *Proc. IEEE Nucl. Sci. Symp., Med. Imag. Conf. Int. Symp. Room-Temp. Semicond. Detectors (NSS MIC RTSD)*, 2023, p. 1. [Online]. Available: https://ieeexplore.ieee.org/document/10337861/

[58] V. Nadig, M. Hornisch, J. Oehm, K. Herweg, V. Schulz, and S. Gundacker, "16-channel SiPM high-frequency readout with time-over-threshold discrimination for ultrafast time-of-flight applications," *EJNMMI Phys.*, vol. 10, no. 1, p. 76, Dec. 2023. [Online]. Available: https://ejnmmiphys.springeropen.com/articles/10.1186/s40658-023-00594-z